Three-dimensional iron sulfide-carbon interlocked graphene composites for high-performance sodium-ion storage

Huang, Wei; Sun, Hongyu; Shangguan, Huihui; Cao, Xianyi; Xiao, Xinxin; Shen, Fei; Mølhave, Kristian; Ci, Lijie; Si, Pengchao; Zhang, Jingdong

Published in:
Nanoscale

Link to article, DOI:
10.1039/C8NR00034D

Publication date:
2018

Document Version
Peer reviewed version

Journal Name

ARTICLE

Three-dimensional iron sulfide-carbon interlocked graphene composites for high-performance sodium-ion storage

Received 00th January 20xx,
Accepted 00th January 20xx

DOI: 10.1039/x0xx00000x

www.rsc.org/

Wei Huang,[a, b] Hongyu Sun,[c] Huihui Shangguan,[a] Xianyi Cao,[b] Xinxin Xiao,[d] Fei Shen,[b] Kristian Mølhave,[c] Lijie Ci,[a] Pengchao Si [*a] and Jingdong Zhang [*b]

Three-dimensional (3D) carbon-wrapped iron sulfide interlocked graphene (Fe_7S_8@C-G) composites for high-performance sodium-ion storage are designed and produced through electrostatic interaction and subsequent sulfurization. The iron-based metal-organic frameworks (MOFs, MIL-88-Fe) interact with graphene oxide sheets to form 3D networks, and carbon-wrapped iron sulfide (Fe_7S_8@C) nanoparticles with high individual-particle conductivity are prepared following a sulfurization process, surrounded by interlocked graphene sheets to enhance the interparticle conductivity. The prepared Fe_7S_8@C-G composites not only have the improved individual-particle and interparticle conductivity to shorten electron/ion diffusion pathways, but also have the enhanced structural stability to prevent the aggregation of active materials and buffer large volume charges during sodiation / desodiation. As a sodium-ion storage material, the Fe_7S_8@C-G composites exhibit a reversible capacity of 449 mA h g^{-1} at 500 mA g^{-1} after 150 cycles and a retention capacity of 306 mA h g^{-1} under a current density of 2000 mA g^{-1}. The crucial factors related to the structural changes and stability during cycles have been further investigated. These results demonstrate that the high-performance sodium-ion storage properties are mainly attributed to the unique designed three-dimensional configuration.

Introduction

The increasing demand for electrical energy storage devices brings great chances and challenges for the secondary battery technology. Lithium ion batteries (LIBs) have been commercialized and widely used for portable electronics since 1990s.[1-5] However, high cost and scarce lithium resources hinder their applications for large-scale energy storage. As an alternative, sodium ion batteries (SIBs) have attracted significant attention over the past five years due to earth-abundance and lower cost of sodium. On the other hand, unsatisfied sodium-ion storage performances were found in SIBs, in contrast to LIBs, which is mainly caused by the obvious ionic size difference (1.02 Å for Na^+ vs. 0.76 Å for Li^+). Particularly, the large size of Na^+ leads to sluggish ion diffusion kinetics and more pronounced volume changes of electrode materials during sodiation / desodiation cycles, resulting in low capacities and inferior cycling stability.[6-11] Thanks to the similar electrochemical properties of Na^+ and Li^+, the well-established design principles of LIBs electrode materials can be transferred to SIB studies.[10,11] For example, nanostructured electrode materials possessing high surface areas are favorable for increasing the contact between electrodes and electrolyte, accommodating the large volume changes during cycles. Further incorporating conductive agents (carbon nanotube, graphene, etc) with the active materials can improve the electrical and ionic conductivity, which is crucial for applications in high-rate cycles.[10,12]

Transition metal sulfides (TMSs) have attracted tremendous interest for SIBs due to the large theoretical capacity (> 400 mA h g^{-1}) and ease of scale-up production.[10,12-15] Iron sulfides (Fe_xS_y) have been recently studied as electrode materials of SIBs.[16-26] High theoretical capacity and low cost make them very competitive compared to other TMSs. The intrinsic shortcomings in Fe_xS_y electrodes, including low electrical conductivity, serious volume expansion and sluggish Na^+ diffusion kinetics during cycles, can be overcome by rational structural and compositional design to achieve high-performance sodium-ion storage. For example, Chen et al. reported FeS_2 microspheres anchored on graphene aerogel with enhanced sodium storage properties, which were attributed to the synergetic effects of FeS_2 microspheres and high electrical conductivity of graphene.[25] Sun and co-workers fabricated carbon nanotube (CNT)-encapsulated $Fe_{1-x}S$ composite, which provided high conductivity paths for electrons/ions and the combined merits

[a] SDU & Rice Joint Center for Carbon Nanomaterials, Key Laboratory for Liquid-Solid Structural Evolution and Processing of Materials, Ministry of Education, School of Materials Science and Engineering, Shandong University, Jinan 250061, P. R. China. Email: pcsi@sdu.edu.cn (P.S.)
[b] Department of Chemistry, Technical University of Denmark, DK-2800 Kongens Lyngby, Denmark. Email: jz@kemi.dtu.dk (J.Z.)
[c] Department of Micro- and Nanotechnology, Technical University of Denmark, DK-2800 Kongens Lyngby, Denmark.
[d] Department of Chemical Sciences and Bernal Institute, University of Limerick, Limerick, Ireland.

Electronic Supplementary Information (ESI) available: XRD patterns, SEM and TEM images, EDS spectra and mapping images, electrochemical data and comparison of electrochemical performance with those reported in literatures. See DOI: 10.1039/x0xx00000x

Please do not adjust margins

of iron sulfide and CNTs, leading to promising capability for SIBs.[26] Most of these studies focused on the combination of Fe_xS_y and conductive agents with less efforts on synergetic effects, including tailoring the spatial organization of Fe_xS_y and conductive agents (interparticle conductivity) as well as Fe_xS_y individual-particle conductivity. Therefore, the enhanced electrode materials can be designed by taking advantage of three-dimensional hierarchical architecture to wrap Fe_xS_y tightly with conductive agents to assist the individual-particle conductivity, with uniformly separated nanoparticles that are interconnected with conductive agents to promote the interparticle conductivity and buffer the volume charges during cycles. Thus promotes the sodium-ion storage in high current density and rate.

Metal-organic frameworks (MOFs) are a class of crystalline porous materials composed of metal units and organic linkers. MOFs are promising precursors to construct the carbon coated metal-based composites with enhanced individual-particle conductivity for electrocatalysis and energy storage.[27-30] Moreover, graphene sheets, which have large surface area, high electrical conductivity and excellent mechanical properties,[31-33] interconnecting individual MOFs derived nanoparticles can enhance interparticle conductivity and accommodate large volume charges during cycles. However, the combination of MOFs and graphene is easily aggregate and lead to inhomogeneous modification during the preparation process. Li et al. reported an electrostatic interaction approach using functionalized carbon spheres as nano-spacers to separate graphene sheets for enhanced supercapacitor performance.[34] Only a few studies focus on three-dimensional hierarchical architecture between MOFs derived composites and graphene for energy storage devices.[35, 36] It is a challenge to construct homogeneously distributed active materials in graphene matrix.

Herein, we have designed three-dimensional (3D) iron sulfide-carbon interlocked graphene (Fe_7S_8@C-G) composites for high-performance sodium-ion storage via electrostatic interaction and subsequent sulfurization. The positive-charge modified iron-based MOFs (MIL-88-Fe) firstly interacted with negative-charge graphene oxide sheets to form three-dimensional networks. By the subsequent sulfurization, MIL-88-Fe transformed to carbon-wrapped iron sulfide (Fe_7S_8@C) nanoparticles to support high individual-particle conductivity, with interlocked graphene oxide (GO) sheets became graphene sheets to assist the interparticle conductivity, generating the Fe_7S_8@C-G composites with the inheritance of original three-dimensional structure. The three-dimensional networks improve the individual-particle and interparticle conductivity to facilitate the transportation of electron and ion, as well as enhance the structural stability to prevent the aggregation of active materials and buffer large volume charges during sodiation / desodiation. The enhanced sodium storage properties of the Fe_7S_8@C-G electrodes with designed three-dimensional architecture are further investigated under electrochemical measurements.

Experimental section

Chemicals

Graphene oxide (GO) was synthesized by a modified Hummers' method.[34] Iron chloride hexahydrate ($FeCl_3{\cdot}6H_2O$, 99%), terephthalic acid ($C_8H_6O_4$, 99%), N, N-Dimethylformamide (DMF, 99.5%), tris (hydroxymethyl) aminomethane (≥ 99.8%), poly (diallyldimethylammonium chloride) (PDDA, MW < 100,000, 35 wt%), sodium chloride (NaCl, 99.5%) were obtained from Aladdin, China. Sulfur powder was purchased from Shanghai Macklin Biochemical Co., Ltd, China. All chemicals were used as received without further purification.

Synthesis of Fe_7S_8@C-G composites.

MIL-88-Fe crystals were prepared according to our previous reported procedure.[5] Briefly, terephthalic acid (0.230 g) and $FeCl_3{\cdot}6H_2O$ (0.374 g) were dissolved in 60 mL DMF, followed with hydrothermal reaction at 150 °C for 2 h. After cooling down to room temperature, the final products were purified with centrifugation and washing with ethanol at least three times. After drying, the MIL-88-Fe crystals were obtained. In order to introduce positive charge on the MIL-88-Fe crystals surface, NaCl (0.173 g), tris-(hydroxymethyl) aminomethane (0.363 g) and PDDA (2.149 g) were dissolved in 150 mL deionized water, in which MIL-88-Fe crystals (0.20 g) were immersed under stirring for 12 h, followed by washing with deionized water more than three times to remove the redundant PDDA. The decorated MIL-88-Fe crystals with positive charge on the surface were mixed with 20 ml GO solution (3 mg/mL) and stirred for 6 h. After freezing-dry process, MIL-88-Fe/GO samples were obtained.

To fabricate Fe_7S_8@C-G composites, the synthesized MIL-88-Fe/GO powder (0.10 g) and sulfur powder (0.40 g) were uniformly mixed, annealed at 600 °C for 6 h under Ar atmosphere. The dark powder (Fe_7S_8@C-G) was collected after cooling down to room temperature. As a control, Fe_7S_8@C composites without the addition of GO precursor were also synthesized accordingly.[5]

Materials characterization.

The crystalline features of the samples were examined by X-ray diffraction (XRD, Miniflex 600). Zeta-potential measurements were analyzed by Zetasizer Nano ZS (Malvern Instruments). Raman spectra were obtained using a Raman spectrometer (Renishaw InVia, 633 nm Laser). X-ray photoelectron spectroscopy (XPS) analysis was carried out on the substrate of silicon slice with a Thermo-Scientific system (Al-Kα radiation, 1484.6 eV). Thermal gravimetric analysis (TGA, Mettler-Toledo TGA/SDTA851e Thermo Analyzer) was performed in air in a temperature range from room temperature to 800 °C with a heating rate of 10 °C min^{-1}. The microstructure and composition analysis were characterized via scanning electron microscope (SEM, HITACHI SU-70, 15 kV; Quanta FEG 200 ESEM, 20 kV), atomic-force microscopy (AFM, Aligent Technology, tapping mode, mica sheet for the substrate), and transmission electron microscopy (TEM, Tecnai G2 T20, 200 kV).

Electrochemical measurements.

The working electrodes were composed of the as-prepared active materials (70 wt%), super P (20 wt%) and polyvinylidene fluoride (PVDF) (10 wt%) mixed in N-methyl-2-pyrrolidone (NMP). The batteries (CR 2016 coin-type cell) were assembled in a glove box under Ar atmosphere at room temperature, using 1.0 M $NaClO_4$ in ethylene carbonate/propylene carbonate (EC: PC =1: 1 wt%) and 5 wt% fluoroethylene carbonate (FEC) as the electrolyte. Metallic

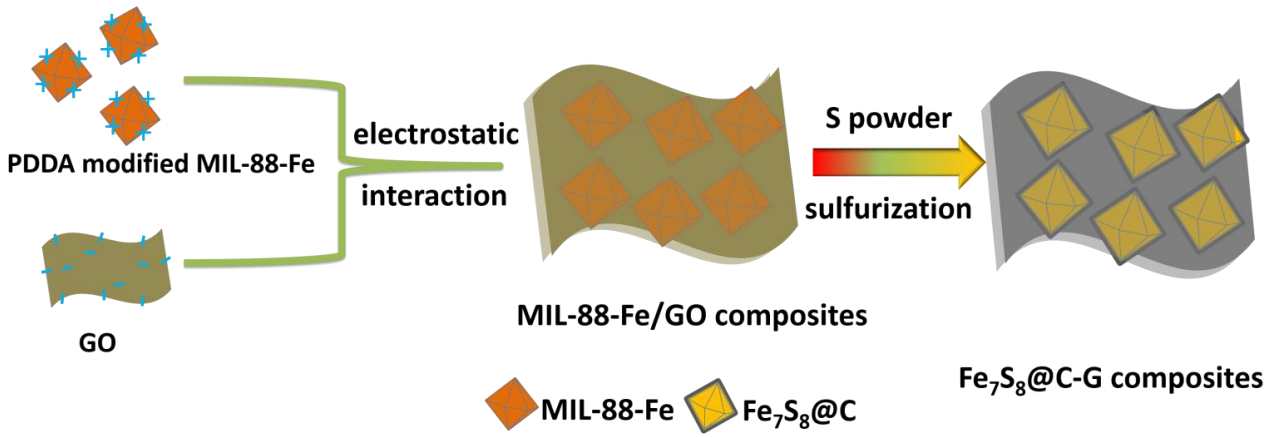

Scheme 1 Schematic illustration of the synthesis process of Fe_7S_8@C-G composites. Not drawn to real scale.

sodium and glass fiber (Whatman, GE Healthcare) were used as the counter electrode and separator, respectively. Galvanostatic charge/discharge test in a voltage range of 0.01-3.0 V was carried out on a Neware-CT-3008 test system (Shenzhen, China). Cyclic voltammograms (CVs) in the voltage window of 0.01-3.0 V at a scan rate of 0.1 mV s^{-1} were conducted using a CHI 660E electrochemical workstation (Shanghai, China). Electrochemical impedance spectroscopy (EIS) in the frequency range of 0.01 to 100 kHz was recorded at the open circuit potential (OCP) using a Metrohm Autolab instrument.

Results and discussion

Structural and component characteristics.

Fe_7S_8@C-G composites were synthesized as illustrated in Scheme 1. First, positive charge was introduced on the surface of MIL-88-Fe crystals in a stirred PDDA solution, the zeta potential (29.8±4.42 mV) of modified MIL-88-Fe crystals solution (Fig.S1 and Table S1) confirmed the positive surface charge.[37] Due to abundant oxygen-containing functional group on the surface of GO sheet, which displayed negative-charge surface.[34] The zeta potential (-46.3±11.2 mV) of as-prepared GO solution further indicated the negative surface charge (Fig.S1 and Table S1). Thus GO sheets tightly interlocked with the activated MIL-88-Fe crystals via electrostatic interaction. Three-dimensional MIL-88-Fe/GO samples were obtained via freezing-dry process. During sulfurization, the iron-based MOFs (MIL-88-Fe) were transformed to carbon-wrapped iron sulfide (Fe_7S_8@C) nanoparticles to support high individual-particle conductivity by sacrificing precursor containing iron units and carbon links, with interconnected graphene sheets reduced from GO sheets, to enhance the interparticle conductivity and structural stability. The final Fe_7S_8@C-G composites inherited the original three-dimensional configuration.

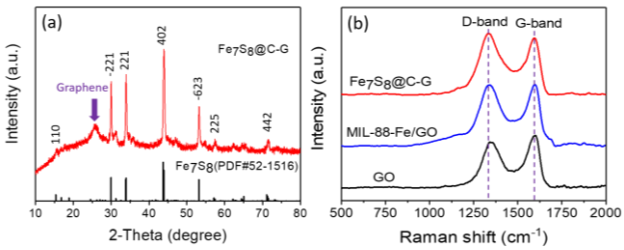

Fig. 1 (a) The XRD pattern of Fe_7S_8@C-G composites. (b) Raman spectra of Fe_7S_8@C-G and MIL-88-Fe/GO composites.

The successful synthesis of Fe_7S_8@C-G composites was firstly confirmed by X-ray diffraction (XRD) analysis. The characteristic peaks (Fig. 1a) matched well with Fe_7S_8 phase (JCPDS no. 52-1516), the corresponding diffraction peaks fit well with (110), (-221), (221), (402), (-623), (225) and (442) planes of pyrrhotite. A broad low-intensity peak in the range of 24-28° (marked by purple arrow) related to the stack of graphene sheets.[32,38] The Raman spectra (Fig. 1b) further indicated the finger-printed signals of graphene. Due to D band is associated with the disordered graphite from the defects and disorders of structures in carbon materials, G band is attributed to the vibration of sp^2 hybridized C-C bond.[39, 40] The I_D/I_G ratio of Fe_7S_8@C-G composites (1.08) was higher than that of MIL-88-Fe/GO (1.00) and GO (0.87) due to the improvement of carbonaceous defects and disorders of graphitized structures, which was attributed to the reduction of GO to graphene sheets and its interaction with MIL-88-Fe crystals.[33,40] Moreover, the locations of D and G bands were 1341.62 & 1598.38 cm^{-1} for MIL-88-Fe/GO and 1344.08 & 1600.81 cm^{-1} for GO, respectively. While, Fe_7S_8@C-G showed red-shifted peaks at 1334.54 cm^{-1} (D band) and 1594.97 cm^{-1} (G band) in comparison to those of MIL-88-Fe/GO and GO, indicating the hybrid structure and electronic interaction between graphene sheets and Fe_7S_8@C nanoparticles rather than simply physical adsorption.[38, 41]

The chemical bonding states of Fe_7S_8@C-G composites were investigated by XPS analysis. All signals originating from expected elements (S, C, O and Fe) were obtained in the survey spectrum (Fig. S2a). Beside, a small peak at ~400 eV was observed in the survey spectrum of Fe_7S_8@C-G corresponding to N 1s, which is attributed to decomposition of the tirs (hydroxymethyl) aminomethane and PDDA in the MIL-88-Fe/GO composites after the electrostatic interaction. In the C 1s region (Fig. S2b), the two peaks at 284.4 and 285.2 eV corresponded to two kinds of carbon bonds (sp^2 and sp^3 bond).[42] Other two peaks at 286.0 and 288.1 eV were assigned to the C-O and C=O bonding, respectively.[25,43] Peaks

at 161.6, 162.6, 163.5 and 164.8 eV of the S 2p spectrum (Fig. S2c) corresponded to S^{2-} and S_n^{2-}, the other peak at 168.4 eV was attributed to oxidized groups (SO_x), indicating partial oxidiation in the surface of composites and the sulfur doping in the graphene sheets.[26, 44, 45] Peaks in the Fe 2p spectrum (Fig. S2d) analysed at 710.9 and 721.5 eV were caused by the Fe^{2+} of composites, peaks at 713.9 and 724.3 eV revealed the presence of Fe^{3+} in the composites, indicating the coexistence of Fe^{2+} and Fe^{3+} in the iron sulfide.[26, 46] The component of Fe_7S_8@C-G was determined by TGA (Fig. S3), which showed one-step increase and multiple steps for weight loss. Firstly, the weight increase in the temperature range of 200 to 320 °C was attributed to partial generation of ferric sulfate.[47] Weight loss increased dramatically in the temperature ranges of 420-520 °C and 540-670 °C, likely due to the conversion of carbon composition to CO_2 and formation of Fe_2O_3 from Fe_7S_8 and $FeSO_4$,[5] respectively. Thus, TGA curve showed a weight loss of 30.8%, the percentage of iron sulfide was calculated to be 80.1% (Fig. S2).

Morphology and microstructure.

The microstructures of the as-prepared MIL-88-Fe crystals, MIL-88-Fe/GO composites and Fe_7S_8@C-G composites were visualized by SEM. The MIL-88-Fe crystals without GO had a bipyramid (or spiral) structure as shown in Fig. S4, representing 788±93 nm in length and 544±101 nm in width. After electrostatic interaction with GO nanosheets, the generated MIL-88-Fe/GO composites (Fig. 2a) showed uniform distribution of MIL-88-Fe crystals interlocked by GO nanosheets into a three-dimensional network structure. After sulfurization, GO transformed to graphene sheets, and irregular Fe_7S_8@C nanoparticles were generated with the inheritance of the morphology and structure of the MIL-88-Fe precursors, leading to well-defined and distributed Fe_7S_8@C nanoparticles with an average size in the range of 100-400 nm interconnected with graphene sheets. Interestingly, the initial three-dimensional network structure simultaneously preserved (Fig. 2b). Energy dispersive spectrometry (EDS) typically revealed the presences of elemental carbon, oxide, sulfur and iron. The obtained atomic ratio of Fe/S of 7:8 further confirmed the formation of Fe_7S_8 (Fig. S5a). Atomic force microscopic (AFM) image of Fe_7S_8@C-G composites (Fig. S5b) distinctly showed the surface micromorphology, consistent with the SEM image (Fig. 2b). The existence of uniformly distributed Fe_7S_8@C nanoparticles in a graphene matrix was thus well confirmed.

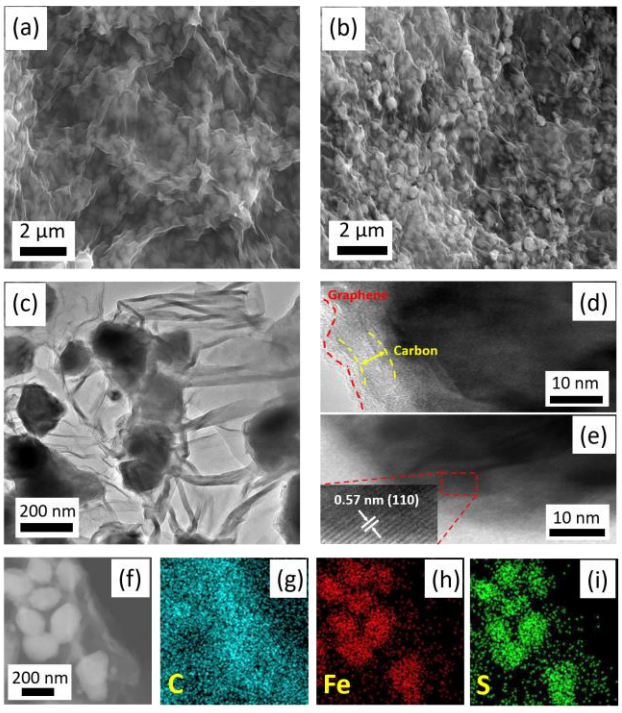

Fig. 2 Morphology and Microscopic Structure: (a) SEM image of MIL-88-Fe/GO composites. (b) SEM image of Fe_7S_8@C-G composites. (c) TEM image of Fe_7S_8@C-G composites. (d, e) HRTEM image of Fe_7S_8@C-G composites. (f-i) EDS elemental mapping images of Fe_7S_8@C-G composites.

TEM image showed the dark Fe_7S_8@C nanoparticles interlocked by light silk-shaped graphene sheets (Fig. 2c). High-resolution transmission electron microscopic (HRTEM, Fig. 3d and 3e) images indicated that Fe_7S_8 nanoparticles were wrapped by amorphous carbon from the carbon links of MIL-88-Fe frameworks, interconnected with graphene sheets. Interplanar spacing of the lattice (Fig. 3e) was measured as 0.57 nm, in accordance with the (110) plane of Fe_7S_8 (JCPDS no. 52-1516).[5,20] The EDS elemental mapping images (Fig. 2f-2i) suggested the homogeneous distribution of carbon (blue), while in the particles iron (red) and sulfur (green) elements, further confirming that Fe_7S_8@C nanoparticles were interconnected by graphene sheets. In contrast, the structure of GO-free bipyramid (or spiral) MIL-88-Fe crystals transformed upon annealing to core-shell nanorods with thin carbon shells (Fig. S6), due to absence of GO in the protocol. Based on the structural and morphological characteristics. Fe_7S_8 nanoparticles were wrapped by amorphous carbon to maintain the high individual-particle conductivity, and homogeneous Fe_7S_8@C nanoparticles interlocked graphene sheets provided excellent interparticle conductivity and structural stability, achieving three-dimensional material design.

Electrochemical behavior and battery performances.

The sodium-ion storage properties of Fe_7S_8@C-G and Fe_7S_8@C composites were investigated in a half-cell configuration. CV curves of the first five cycles of Fe_7S_8@C-G composites in a voltage range of 0.01–3.0 V with a scanning rate of 0.1 mV s^{-1} were shown in Fig. 3a. In the first cathodic scan, three peaks were observed at 1.08, 0.81 and 0.24 V, respectively. The peak at 1.08 V corresponded to the formation of solid electrolyte interface (SEI) film. The peaks at 0.81 and 0.24 V were attributed to the generation of Na_xFeS_2 and Fe & Na_2S, respectively.[20, 25, 26] In the initial anodic scan, two peaks were observed at 1.42 and 1.85 V arising from the conversion of Fe to Na_2FeS_2 and Na_xFeS_2.[22, 25, 26] The CVs overlapped well each other from the second scan afterwards, which demonstrates a good superior electrochemical stability and reversibility during cycles. In comparison, the CVs of Fe_7S_8@C composites (Fig. S7a) gave an irreversible decrease, which is due to the decomposition of active materials, revealing the expected instability of Fe_7S_8@C electrodes during sodiation / desodiation.[38] The related sodiation / desodiation reaction could be described as following.[20,22,25,26]

$Fe_7S_8 + 4xNa^+ + 4xe^- \rightarrow 4Na_xFeS_2 + 3Fe$ (1)

$Na_xFeS_2 + (4-x)Na^+ + (4-x)e^- \rightarrow 2Na_2S + Fe$ (2)

$2Na_2S + Fe \leftrightarrow Na_2FeS_2 + 2Na^+ + 2e^-$ (3)

$Na_2FeS_2 \leftrightarrow Na_xFeS_2 + (2-x)Na^+ + (2-x)e^-$ (4)

Fig. 3b showed the galvanostatic discharge / charge profiles of the first three, 10th and 20th cycles of Fe_7S_8@C-G composites at a current density of 100 mA g^{-1}. The distinct voltage slopes in the first cycle were consistent with the peaks observed in CVs (Fig. 3a), the initial discharge and charge capacity were calculated to be 714 and 426 mA h g^{-1}, respectively. The relatively low initial Coulombic efficiency (60 %) was attributed to the formation of SEI films on the surface of active materials and the irreversible partial decomposition of the electrolyte.[20, 21] After the initial cycle, the discharge / charge curves overlapped well with a Coulombic efficiency over 94%, indicating a superior cycling stability after initial activation. In contrast, the initial discharge and charge capacity of Fe_7S_8@C (Fig. S7b) were 836 and 472 mA h g^{-1} with a low initial Coulombic efficiency of 56%, respectively. Obviously, no overlapping curves (Fig. S6b) were observed, revealing a weak cycling stability.

The cycling performance of Fe_7S_8@C-G and Fe_7S_8@C composites at 100 mA g^{-1} was shown in Fig. 3c. Fe_7S_8@C-G delivered a lower initial discharge / charge capacity than that of Fe_7S_8@C, which was attributed to the lower percentage of Fe_7S_8 in Fe_7S_8@C-G composites (80.1 %) than that in Fe_7S_8@C composites (87 %) due to the modification of graphene sheets.[5] it was also observed that there was a gradual capacity increase for Fe_7S_8@C-G during cycling process. Then, the discharge capacity of Fe_7S_8@C-G became stable at 478 mA h g^{-1} after 100 cycles, with a capacity retention of 67%. The observation is assigned to the long-term activation of electrode materials for the structural rearrangement and more active sites for sodiation / desodiation would be provided due to the decrease in Fe_7S_8@C particles sizes during cycling process. [5, 26] Besides, the flexible graphene sheets effectively prevented the further cracks of Fe_7S_8@C particles, thus maintained superior cycling performance. Comparatively, the discharge capacity of Fe_7S_8@C (Fig. 3c) exhibited a value of 229 mA h g^{-1} after 100 cycles, with a low capacity retention of 27%. The capacity loss of Fe_7S_8@C was attributed to

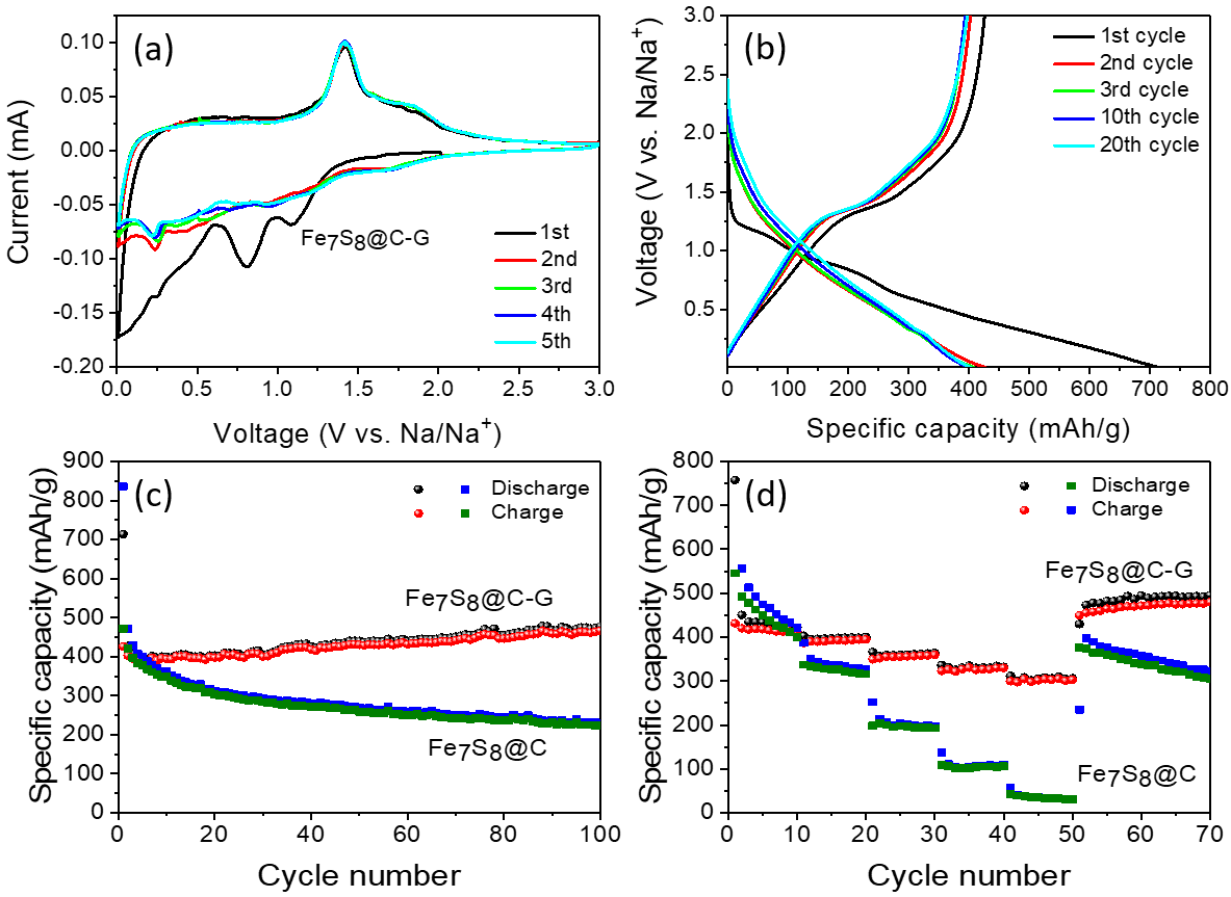

Fig. 3 (a) Cyclic voltammograms of the first five cycles for Fe_7S_8@C-G composites in a voltage range of 0.01–3.0 V with a scanning rate of 0.1 mV s^{-1}. (b) Galvanostatic discharge/charge profiles of the first three, 10th and 20th cycles for Fe_7S_8@C-G composites at a current density of 100 mA g^{-1}. (c) Cycling performance of Fe_7S_8@C-G and Fe_7S_8@C composites at a current rate of 100 mA g^{-1}. (d) Rate capability of Fe_7S_8@C-G and Fe_7S_8@C composites at different current densities of 100, 200, 500, 1000, 2000 and 100 mA g^{-1} with the numbers noted in (d).

the continuous cracking of Fe_7S_8@C composites, thin carbon shell was not efficient to restrain the pulverization of Fe_7S_8@C composites. Fe_7S_8@C-G composites (Fig. 3d) registered capacities of 463, 398, 361, 332, 306 mA h g^{-1} at current densities of 100, 200, 500, 1000, 2000 mA g^{-1}. When the current density reduced back to 100 mA g^{-1} after 50 cycles, the capacity recovered to 495 mA h g^{-1} after 70 cycles. In comparison, Fe_7S_8@C composite (Fig. 3d) displayed capacities of 535, 341, 207, 110, 37 mA h g^{-1} at current densities of 100, 200, 500, 1000, 2000 mA g^{-1}. When the current density was set back to 100 mA g^{-1} after 50 cycles, the capacity only retained 323 mA h g^{-1} after 70 cycles. Clearly, superior rate capability of Fe_7S_8@C-G composites revealed that graphene sheets played a crucial role to interlock the individual Fe_7S_8@C nanoparticles for promoting the interparticle conductivity and accommodating large volume charges during high-rate cycles.

Long-term cycling performance of Fe_7S_8@C-G (Fig. 4a) and Fe_7S_8@C composites (Fig. 4b) at a higher current density of 500 mA g^{-1} were further conducted. Fe_7S_8@C-G composites delivered a high reversible discharge capacity of 449 mA h g^{-1} after 150 cycles, with a Coulombic efficiency of over 96 % after the first three cycles. In contrast, the Fe_7S_8@C composites exhibited a low reversible discharge capacity of 81 mA h g^{-1} after 150 cycles. High-performance sodium ion storage during high current-density cycles was attributed to the three-dimensional material structural design. Moreover, the sodium storage properties of the synthesized Fe_7S_8@C-G composites are superior or comparable to recent reports on iron sulfides electrodes for SIBs (Table S2). For example, Qu and co-workers reported iron sulfide coated by carbon layer(Fe_7S_8/C) composites for sodium storage, which delivered a capacity of 352 mA h g^{-1} at 500 mA g^{-1} after 100 cycles.[23] Yu et al. demonstrated FeS@C-carbon cloth (CC) as flexible electrodes for sodium storage, which exhibited a capacity of 365 mA h g^{-1} at 91.35 mA g^{-1} after 100 cycles.[24] The Fe_7S_8@C-G composites electrodes reported here gave superior electrochemical performance.

For a better understanding of the promising sodium-ion storage of Fe_7S_8@C-G composites, EIS measurements were carried out. Fig. 4c showed the Nyquist impedance plots of Fe_7S_8@C-G composite and Fe_7S_8@C composites before cycling. In the plots, the medium-frequency semicircle corresponded to the impedance of charge-transfer resistance (R_{ct}) between electrode and electrolyte.[38, 48] Lower R_{ct} of Fe_7S_8@C-G composites than that of Fe_7S_8@C composites was found, thus indicating Fe_7S_8@C nanoparticles interlocked the flexible graphene sheets to construct the high conductive three-dimensional networks. In addition, flexible graphene sheets served as the linker and electrical conductor to interconnect the individual Fe_7S_8@C nanoparticles for enhanced interparticle conductivity, efficiently promoting the charge transfer kinetics. Moreover, 5 and 10 cycles coin cell of Fe_7S_8@C-G composites (Fig. 4d) exhibited a smaller R_{ct} than that of fresh, respectively. The decrease of semicircles is likely due to the lattice

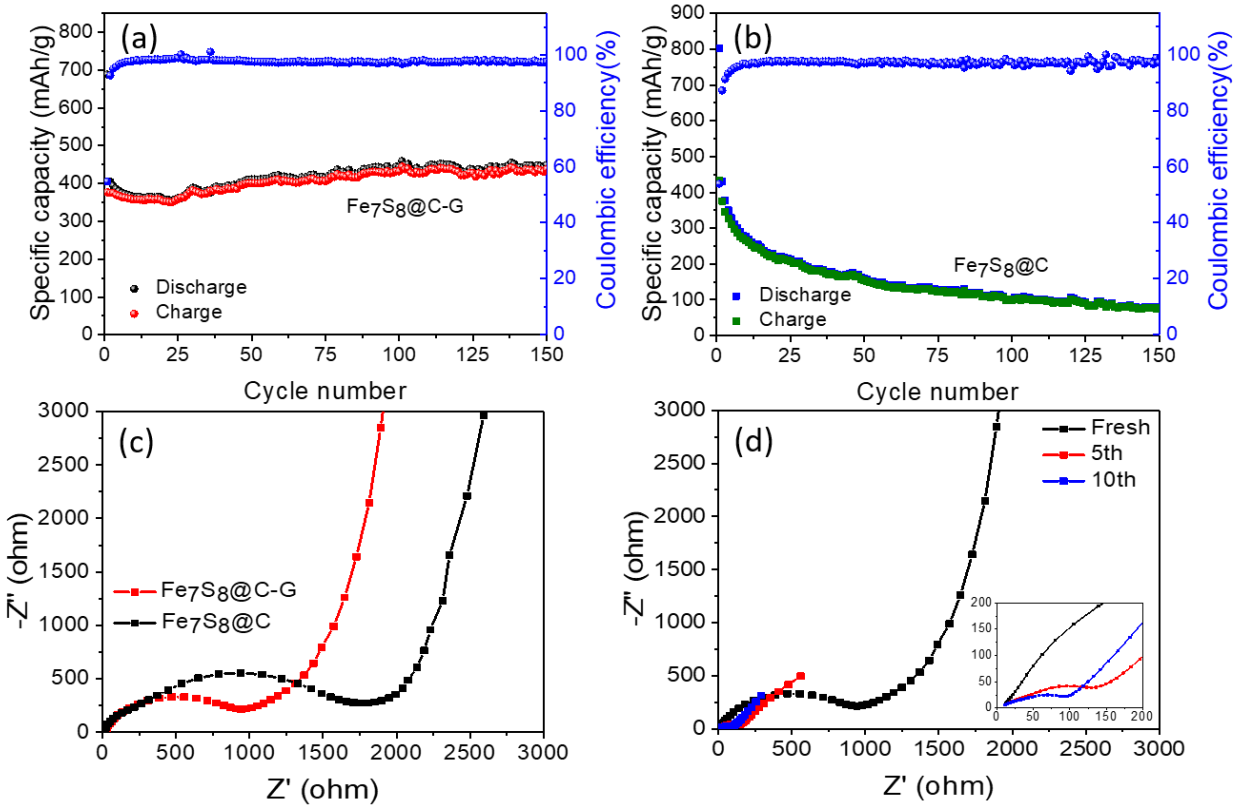

Fig. 4 The cycle performance of (a) Fe_7S_8@C-G composites and (b) Fe_7S_8@C composites at a current rate of 500 mA g^{-1}. (c) Nyquist impedance plots of Fe_7S_8@C-G composites and Fe_7S_8@C composites before cycling. (d) Nyquist impedance plot of Fe_7S_8@C-G composites (fresh, after 5 and 10 cycles).

expansion and surface activation of electrode, greatly enhancing the charge transfer kinetics.[22, 49] The medium-frequency semicircles of Fe_7S_8@C-G composites after 5 and 10 cycles maintained the low charge-transfer resistance, revealing the structural stability for stable cycling performance.

The morphologies of Fe_7S_8@C and Fe_7S_8@C-G electrodes after 100 discharge / charge cycles at 100 mA g^{-1} were investigated. Cracks were observed on the surface of Fe_7S_8@C electrode (Fig. S8a), whereas, no cracking was found on the Fe_7S_8@C-G electrode (Fig. S8b), suggesting the buffering function and operational stability of graphene based composite during sodiation / desodiation. TEM image (Fig. 5a) further revealed that Fe_7S_8@C electrode materials were pulverized and aggregated seriously after 100 cycles at 100 mA g^{-1}. In comparison, Fe_7S_8@C nanoparticles interlocked tightly by graphene without pulverization were observed in Fig. 5b, further proving the good structural stability of Fe_7S_8@C-G composites for superior cycling performance. These features were schematically illustrated in Fig. 5c and 5d. The Fe_7S_8@C electrode (Fig. 5c) exhibited a large volume expansion during cycles, thin carbon shell was not sufficient to maintain the structural stability, and then caused the cracks and pulverization during the long-term sodiation / desodiation, [20, 50] finally leading to capacity loss (Fig. 3c). The Fe_7S_8@C-G electrode (Fig. 5d) exhibited good structural ability during cycles, due to that the flexible graphene sheets greatly improved the dispersion and interparticle conductivity of Fe_7S_8@C nanoparticles, effectively prevented Fe_7S_8@C nanoparticles from decomposition and aggregation and buffered the volume changes during the long-term sodiation / desodiation. Thus, such three-dimensional material (Fe_7S_8@C-G composites) enhanced the sodium-ion storage capacity, cycling performance and rate capability (Fig. 3c, 3d and 4a).

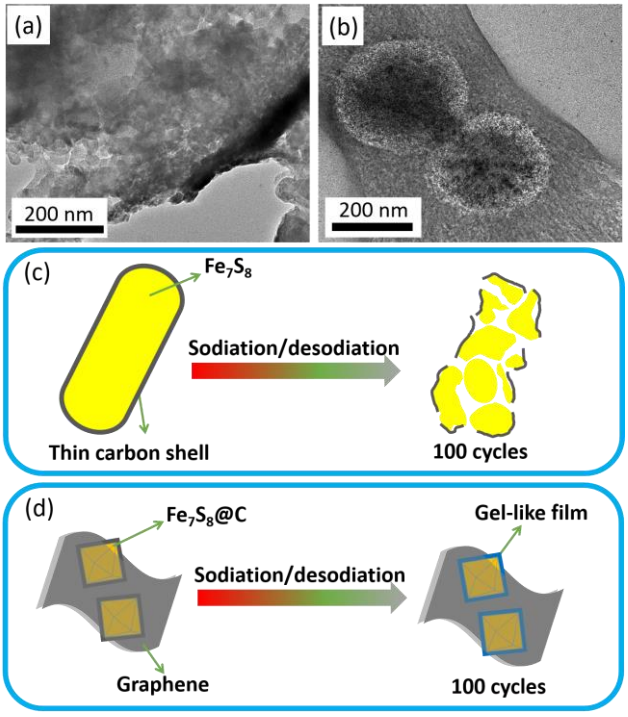

Fig. 5 (a, b) TEM images of Fe_7S_8@C (a) and Fe_7S_8@C-G (b) electrode materials after 100 charge-discharge cycles at 100 mA g^{-1}. (c, d) Schematic illustration of the sodiation/desodiation for Fe_7S_8@C (c) and Fe_7S_8@C-G (d) electrode materials after 100 charge-discharge cycles at 100 mA g^{-1}. Not drawn to real scale.

Conclusion

We have successfully developed a 3D iron sulfide-carbon interlocked graphene composites (Fe_7S_8@C-G) by an electrostatic interaction strategy, followed with a sulfurization process. The iron-based MOFs (MIL-88-Fe) changed into carbon-wrapped iron sulfide (Fe_7S_8@C) nanoparticles to support high individual-particle conductivity, with interconnected GO sheets reduced into graphene sheets to enhance the interparticle conductivity and buffer the large volume changes during sodiation / desodiation, generating the Fe_7S_8@C-G composites with the inheritance of original 3D structure. Utilized for sodium-ion storage, the 3D networks facilitated the transportation of electron / ion, and promoted structural stability of electrodes, thus improving the cycling performance and rate capability. The prepared Fe_7S_8@C-G composites exhibit a superior reversible capacity of 449 mA h g^{-1} at 500 mA g^{-1} after 150 cycles and an impressive retention capacity of 306 mA h g^{-1} under the current density of 2000 mA g^{-1}. These results demonstrated that the composites can be used for high-performance sodium-ion storage, and the structural design inspires advances for SIBs.

Acknowledgements

Finance support from Danish Council for Independent Research (DFT-1335-00330) to J.Z., China Scholarship Council for a PhD scholarship (201706220080) to W.H., is greatly appreciated. L.C. and P. S. are supported by Startup Funding of Distinguished Professorship of “1000 Talents Program” (31270086963030), Shandong Provincial Science and Technology Major Project (2015ZDZX11008, 2015GGE27286, 2016GGX104001). We appreciate constructive suggestions and discussion from Professor Jens Ulstrup.

References

1 M. Armand and J.-M. Tarascon, *Nature* 2008, **451**, 652-657.
2 B. Dunn, H. Kamath, J.-M. Tarascon, *Science* 2011, **334**, 928-935.
3 C. Wang, M. Lan, Y. Zhang, H. Bian, M.-F. Yuen, K. K. Ostrikov, J. Jiang, W. Zhang, Y. Y. Li, J. Lu, *Green Chem*. 2016, **18**, 3029-3039.
4 H. Sun, Y. Zhao, K. Mølhave, M. Zhang, J. Zhang, *Nanoscale* 2017, **9**, 14431-14441.
5 W. Huang, S. Li, X. Cao, C. Hou, Z. Zhang, J. Feng, L. Ci, P. Si, Q. Chi, *ACS Sustainable Chem. Eng.* 2017, **5**, 5039-5048.
6 M. D. Slater, D. Kim, E. Lee, C. S. Johnson, *Adv. Funct. Mater.* 2013, **23**, 947-958.
7 V. Palomares, P. Serras, I. Villaluenga, K. B. Hueso, J. Carretero-González, T. Rojo, *Energy Environ. Sci.* 2012, **5**, 5884-5901.

8 N. Yabuuchi, K. Kubota, M. Dahbi, S. Komaba, *Chem. Rev.* 2014, **114**, 11636-11682.
9 D. Kundu, E. Talaie, V. Duffort, L. F. Nazar, *Angew. Chem. Int. Ed.* 2015, **54**, 3431-3448.
10 Z. Hu, Liu, Q.; Chou, S.-L.; Dou, S.-X. *Adv. Mater.* 2017, 1700606.
11 C. Grey, J.M. Tarascon, *Nat. Mater.* 2017, **16**, 45-56.
12 Y. Zhang, Q. Zhou, J. Zhu, Q. Yan, S. X. Dou, W. Sun, *Adv. Funct. Mater.* 2017, **27**, 1702317.
13 T. Zhou, W. K. Pang, C. Zhang, J. Yang, Z. Chen, H. K. Liu, Z. Guo, *ACS Nano* 2014, **8**, 8323-8333.
14 D. Su, S. Dou, G. Wang, *Adv. Energy Mater.* 2015, **5**, 1401205.
15 L. Zhou, K. Zhang, J. Sheng, Q. An, Z. Tao, Y.-M. Kang, J. Chen, L. Mai, *Nano Energy* 2017, **35**, 281-289.
16 T.B. Kim, W.H. Jung, H.S. Ryu, K.W. Kim, J.H. Ahn, K.K. Cho, G.B. Cho, T.H. Nam, I.S. Ahn, H.J. Ahn, *J. Alloys Compd.* 2008, **449**, 304-307.
17 T.B. Kim, J.W. Choi, H.S. Ryu, G.B. Cho, K.W. Kim, J.H. Ahn, K.K. Cho, H.J. Ahn, *J. Power Sources* 2007, **174**, 1275-1278.
18 Y. Zhu, L. Suo, T. Gao, X. Fan, F. Han, C. Wang, *Electrochem. Commun.* 2015, **54**, 18-22.
19 Z. Hu, Z. Zhu, F. Cheng, K. Zhang, J. Wang, C. Chen, J. Chen, *Energy Environ. Sci.* 2015, **8**, 1309-1316.
20 Y.-X. Wang, J. Yang, S.-L. Chou, H. K. Liu, W.-x. Zhang, D. Zhao, S. X. Dou, *Nat. Commun.* 2015, **6**, 8689.
21 Z.-G. Wu, J.-T. Li, Y.-J. Zhong, J. Liu, K. Wang, X.-D. Guo, L. Huang, B.-H. Zhong, S.-G. Sun, *J. Alloys Compd.* 2016, **688**, 790-797.
22 S. Li, B. Qu, H. Huang, P. Deng, C. Xu, Q. Li, T. Wang, *Electrochim. Acta* 2017, **247**, 1080-1087.
23 W. Chen, S. Qi, M. Yu, X. Feng, S. Cui, J. Zhang, L. Mi, *Electrochim. Acta* 2017, **230**, 1-9.
24 X. Wei, W. Li, J.-a. Shi, L. Gu, Y. Yu, *ACS Appl. Mater. Interfaces* 2015, **7**, 27804-27809.
25 W. Chen, S. Qi, L. Guan, C. Liu, S. Cui, C. Shen, L. Mi, *J. Mater. Chem. A* 2017, **5**, 5332-5341.
26 Y. Xiao, J.-Y. Hwang, I. Belharouak, Y.-K. Sun, *ACS Energy Lett.* 2017, **2**, 364-372.
27 H. Li, M. Eddaoudi, M. O'Keeffe, O. M. Yaghi, *Nature* 1999, **402**, 276-279.
28 B. Y. Guan, X. Y. Yu, H. B. Wu, X. W. D. Lou, *Adv. Mater.* 2017, 1703614.
29 L. Wang, Y. Han, X. Feng, J. Zhou, P. Qi, B. Wang, *Coord. Chem. Rev.* 2016, **307**, 361-381.
30 L. Yu, H. B. Wu, X. W. D. Lou, *Acc. Chem. Res.* 2017, **50**, 293-301.
31 A. K. Geim, K. S. Novoselov, *Nat. Mater.* 2007, **6**, 183-191.
32 G. Zhou, D.-W. Wang, F. Li, L. Zhang, N. Li, Z.-S. Wu, L. Wen, G. Q. Lu, H.-M. Cheng, *Chem. Mater.* 2010, **22**, 5306-5313.
33 M. Zhang, C. Hou, A. Halder, J. Ulstrup, Q. Chi, *Biosens. Bioelectron.* 2017, **89**, 570-577.
34 C. X. Guo, C. M. Li, *Energy Environ. Sci.*, 2011, **4**, 4504-4507.
35 X. Cao, B. Zheng, X. Rui, W. Shi, Q. Yan, H. Zhang, *Angew. Chem. Int. Ed.* 2014, **126**, 1428 –1433.
36 X. Xu, W. Shi, P. Li, S. Ye, C. Ye, H. Ye, T. Lu, A. Zheng, J. Zhu, L. Xu, M. Zhong, X. Cao, *Chem. Mater.* 2017, **29**, 6058−6065.
37 H. Ai, S. A. Jones, M. M. de Villiers, Y. M. Lvov, J. Controlled Release, *2003*, **86**, 59-68.
38 W. Huang, X. Xiao, C. Engelbrekt, M. Zhang, S. Li, J. Ulstrup, L. Ci, J. Feng, P. Si, Q. Chi, *Mater. Chem. Front.* 2017, **1**, 1185-1193.
39 F. Tuinstra, J. L. Koenig, *J. Chem. Phys.* 1970, **53**, 1126-1130.
40 O. Akhavan, M. Abdolahad, A. Esfandiar, M. Mohatashamifar, *J. Phys. Chem. C* 2010, **114**, 12955-12959.
41 E. Gao, W. Wang, M. Shang, J. Xu, *Phys. Chem. Chem. Phys.* 2011, **13**, 2887-2893.
42 D. Yuan, X. Yuan, W. Zou, F. Zeng, X. Huang, S. Zhou, *J. Mater. Chem.* 2012, **22**, 17820-17826.
43 Y. Zhao, H. Sun, L. M. Liu, R. Zong, H. Cao, Z. Zhang, X. Wang, J. Luo, J. Zhu, *Small* 2015, **11**, 1512-1518.
44 E. Shangguan, L. Guo, F. Li, Q. Wang, J. Li, Q. Li, Z. Chang, X.-Z. Yuan, *J. Power Sources* 2016, **327**, 187-195.
45 S. Yang, L. Zhi, K. Tang, X. Feng, J. Maier, K. Müllen, *Adv. Funct. Mater.* 2012, **22**, 3634–3640.
46 A. Śliwak, A. Moyseowicz, G. Gryglewicz, *J. Mater. Chem.A* 2017, **5**, 5680-5684.
47 P. Masset, J.-Y. Poinso, J.-C. Poignet, *J. Therm. Anal. Calorim.* 2006, **83**, 457-462.
48 J. T.S. Irvine, D. C. Sinclair, A. R. West, *Adv. Mater.* 1990, **2**, 132-138.
49 Y. Zhu, Y. Wen, X. Fan, T. Gao, F. Han, C. Luo, S.-C. Liou, C. Wang, *ACS Nano* 2015, **9**, 3254-3264.
50 Z. Li, L. Yin, *J. Mater. Chem. A* 2015, **3**, 21569-21577.

